PCCP

PAPER

View Article Online
View Journal | View Issue

Cite this: *Phys. Chem. Chem. Phys.*, 2018, **20**, 17105

Lead (Pb) interfacing with epitaxial graphene†

Ivan Shtepliuk, *[ab] Mikhail Vagin,[a] Ivan G. Ivanov,[a] Tihomir Iakimov,[a] G. Reza Yazdi[a] and Rositsa Yakimova[a]

Received 20th March 2018,
Accepted 29th May 2018

DOI: 10.1039/c8cp01814f

rsc.li/pccp

Here, we report the electrochemical deposition of lead (Pb) as a model metal on epitaxial graphene fabricated on silicon carbide (Gr/SiC). The kinetics of electrodeposition and morphological characteristics of the deposits were evaluated by complementary electrochemical, physical and computational methods. The use of Gr/SiC as an electrode allowed the tracking of lead-associated redox conversions. The analysis of current transients passed during the deposition revealed an instantaneous nucleation mechanism controlled by convergent mass transport on the nuclei locally randomly distributed on epitaxial graphene. This key observation of the deposit topology was confirmed by low values of the experimentally-estimated apparent diffusion coefficient, Raman spectroscopy and scanning electron microscopy (SEM) studies. First principles calculations showed that the nucleation of Pb clusters on the graphene surface leads to weakening of the interaction strength of the metal–graphene complex, and only spatially separated Pb adatoms adsorbed on bridge and/or edge-plane sites can affect the vibrational properties of graphene. We expect that the lead adatoms can merge in large metallic clusters only at defect sites that reinforce the metal–graphene interactions. Our findings provide valuable insights into both heavy metal ion electrochemical analysis and metal electroplating on graphene interfaces that are important for designing effective detectors of toxic heavy metals.

1. Introduction

It has long been recognised that 0.6% of the global burden of disease is related to Pb (lead) contamination.[1] Being a cumulative toxin, lead exposure has the most adverse effects on children[2,3] and pregnant women,[4] causing neurological disturbances and a decrease of the intelligence quotient. Therefore, the fast and real-time detection of Pb in drinking water and in the environment is one of the important challenges in ecology and healthcare. Due to the low-cost and portability, electrochemical stripping voltammetry is a promising technique for the selective and reliable detection of extremely low Pb concentrations. The core of this technique is the working electrode, playing the role of the main component of the electrochemical cell. In this context, the selection of the appropriate working electrode material with desirable redox behaviour towards Pb (including fast charge transfer and high sorption/desorption rate) and a favourably wide potential window is crucial for designing a high-performance discriminating electrochemical cell with reproducible characteristics and a low detection limit. Graphitic materials are commonly used electrochemical electrodes. Among them, large area graphene formed by the high-temperature thermal decomposition of Si-face SiC(0001) in an argon atmosphere[5,6] has recently received special attention for application as a working electrode[7–10] due to its extreme smoothness yielding high signal-to-noise ratios that are beneficial for electroanalysis of heavy metals, high electron-transfer rate, large surface area and unique electronic properties.[11–13] Thus, any experimental knowledge about the specific interaction between Pb species and epitaxial graphene at the early stages of the deposition of lead is very valuable for elucidating the nature of the sensing mechanisms underlying the electrochemical detection of Pb ions in aqueous solutions and for better understanding the ways to achieve enhanced performance of electrochemical sensors. In light of this necessity, there is a high demand for the development of effective techniques of Pb deposition and understanding the phenomena occurring at the metal/solid interfaces. In this regard, electroplating is an attractive approach because it is an excellent tool for controlling the interface structure.[14]

Our theoretical predictions on the behaviour of Pb on graphene imply the feasibility of using graphene-family materials for working electrode fabrication. It was shown that Pb species tend to bind strongly with free-standing graphene.[15,16] Acting as electron-donating impurities, Pb atoms induce an observable

[a] *Department of Physics, Chemistry and Biology, Linköping University, SE-58183, Linköping, Sweden. E-mail: ivan.shtepliuk@liu.se*
[b] *Frantsevich Institute for Problems of Materials Science, NASU, 03680, Kyiv-142, Ukraine*

† Electronic supplementary information (ESI) available. See DOI: 10.1039/c8cp01814f

shift of the Dirac point of graphene, while the van der Waals interaction between other metals, *e.g.* Cd (Hg) and graphene, has a negligible effect on the band structure. Taking the aforementioned discussion into account, we anticipate that graphene and more specifically graphene on SiC (Gr/SiC) as the working electrode can be used for lead electroplating, which is expected to shed light on the interaction of Pb with this graphene and to help in understanding the mechanism of Pb detection in an electrochemical sensor.

In this report, we gain understanding of the aspects of Pb interfacing with Gr/SiC using electrochemical methods, as well as Raman spectroscopy and scanning electron microscopy (SEM). The results are compared with the first principles calculations.

2. Experimental details and methodology

2.1 Electrochemical measurements

The electrochemical measurements were carried out at room temperature using a computer-controlled potentiostat (Autolab, EcoChemie, Netherlands). The three-electrode electrochemical cell composed of graphene-covered 4H-SiC as the working electrode, platinum wire as the counter electrode and the underlying base for the silver–silver chloride (Ag needle, which was anodically treated in 3 M KCl) reference electrode were used. The electrochemical cell was a plastic box with a volume of 300 μL and there was a small hole in the central part of this box. The Gr/SiC sample was fixed under the hole with the o-ring using screws on the lid. A dry contact to the Gr/SiC was formed by using an aluminum adhesive. The mounted sample was kept inside the cell during all electrochemical measurements in order to avoid sample drift. The electrochemical reactions took place on the hole of 3.1 mm^2 area. A detailed description of the design of the electrochemical cell can be found elsewhere.[10] Prior to Pb electrodeposition, we used the cyclic voltammetry technique to define the working potential window of epitaxial graphene and the onset of hydrolysis. For this aim, the working electrode potential was scanned within the negative potential region from −0.9 V to 0 V in 0.1 M acetate buffer solution at a scan rate of 20 mV s^{-1}. In the next stage, we studied the redox reactions involving Pb species by analysing the cyclic voltammograms. Finally, to elucidate the kinetics of Pb, we recorded the current–time transients during the electrodeposition of lead on graphene-covered SiC. In this regard, the Scharifker–Hills theory was applied to determine the nucleation mechanism. All suprapure chemicals and reagents were purchased from Sigma Aldrich. The buffer solution (0.1 mol L^{-1}) was prepared with $HClO_4$ and Milli-Q-water. 0.1 mM Pb^{2+} ion solution was prepared in 0.1 M buffer electrolyte using metal salts, namely lead(II) nitrate (purity of $Pb(NO_3)_2$ is higher than 99%).

2.2 Epitaxial graphene electrode

Epitaxial graphene on SiC (Gr/SiC) was prepared using high temperature thermal decomposition of the silicon-terminated silicon carbide substrate (7 × 7 mm^2 semi-insulting Si-face 4H-SiC) in an argon atmosphere.[17] According to optical reflectance mapping,[18] more than 70% of the measured sample area consisted of monolayer graphene, while the contribution from bilayer graphene is less than 30%. It should be mentioned that the graphene layer on the SiC template exhibits a terrace-stepped morphology, due to the unintentional misorientation of the SiC substrate and, respectively, a natural step bunching. Graphene monolayer covers the terraces and most of the steps on the SiC surface, but sometimes bilayer inclusions form at the step edges. Such a diversity in thickness allows us to consider both monolayer and bilayer graphene as possible surfaces of the working electrode. But, due to the large areas of monolayer in our sample, we anticipate that the adsorption events will mostly occur on this surface.

2.3 SEM and Raman measurements

To study the size of Pb electrodeposits and to characterize the sample microstructures after the electrochemical studies, we used SEM in a Leo 1550 Gemini SEM at an operating voltage ranging from 10 kV to 20 kV and a standard aperture value of 30 μm. In addition to the above-mentioned reflectance mapping used to obtain the number of graphene layers, Raman mapping on selected areas was employed before and after electrodeposition of lead. The Raman spectra were measured using a micro-Raman setup based on a monochromator (Jobin-Yvon, model HR460) equipped with a CCD camera. The objective lens has a magnification of 100× and a numerical aperture of NA = 0.95, resulting in an ∼0.85 μm diameter of the laser spot on the sample surface. A 532 nm diode-pumped solid-state laser with 17 mW power was used as an excitation source. The spectral resolution of the system is ∼5.5 cm^{-1}.

2.4 DFT calculations

When adsorbed on the graphene surface, heavy Pb adatoms modify the in-plane C–C bond lengths and, consequently, the frequencies of each oscillator. All these changes manifest themselves in the Raman spectra. First principles calculations were performed to investigate the effect of lead species on the Raman spectra of graphene. All calculations were made within the framework of density functional theory (DFT), as implemented in the Gaussian 09 package.[19] We consider zigzag-edged nano-sized graphene ($C_{54}H_{18}$, circumcoronene) as a model. Being planar polycyclic aromatic hydrocarbons (PAHs) with only benzenoid hexagonal rings, circumcoronene can be regarded as a suitable structure to mimic the vibrational properties of graphene. It was previously reported that theoretically calculated D and G bands of $C_{54}H_{18}$ can correlate with the same features observed in defective graphene.[20] In our calculations, the geometry of graphene before and after interaction with neutral Pb species was fully optimized at the PBE1PBE-D3 level of theory,[21] with consideration of the dispersion correction and using the default convergence criteria. The 6-311G(d,p) basis set was used for carbon and passivating hydrogen atoms, while a basis set developed by the Stuttgart–Dresden–Bonn group was applied for the Pb atom.[22] Raman spectra were computed at the same DFT level. To make the theoretical analysis tractable and to reduce

the overall time of DFT calculations, three simplifying assumptions were used. First, we neglect the effect of the SiC substrate on the vibrational properties of graphene, although the lattice mismatch between the graphene layer and SiC may cause strain, thereby leading to a shift of the characteristic modes. Since this shift is not influenced by the adsorbed species, we investigate only the adsorbate-induced relative changes in the Raman spectra of graphene. Secondly, due to the limitations of the theoretical approach related to the second-order Raman scattering process, we consider only the first order D and G modes (the latter is Raman-active, whereas the D-mode is forbidden in the perfect graphene crystal and needs defects, *e.g.*, edges, for its activation). Since our main aim here is to understand the behavior of the Pb species on graphene, we can, without loss of generality, focus on the analysis of these two phonon modes and their relationship correlated with the degree of graphene disorder. Since the edge length to surface area ratio in the nano-sized graphene patch is larger than that in an infinite graphene sheet, we expect the D mode to dominate over the G mode.

3. Results and discussion

3.1 Raman analysis – theory and experiment

A key point in analysing Pb behaviour on the graphene electrode is to understand the nature of the specific interaction between the Pb species and sp^2-hybridized carbon. The interaction strength is the main factor that is responsible for the diffusion, kinetics and nucleation of Pb species. Furthermore, the binding ability of graphene towards Pb unambiguously defines the electrochemical response of the corresponding working electrode regarding reliable and selective lead detection. Therefore, understanding the surface reactions at the graphene interface is a very important task to describe the sensing mechanism. Addressing this challenge requires a comprehensive characterization of the working electrode material (Gr/SiC) before and after Pb adsorption events. Here, we use Raman spectroscopy to monitor the phenomena observed by electrochemical methods (Pb adsorption/desorption on the graphene/SiC working electrode) and the binding of Pb adatoms to epitaxial graphene at critically low concentrations.

Prior to Raman measurements, we performed reflectance mapping to get information on the number of graphene layers. The optical reflectance maps (not shown here) reflect the distribution of regions with different thicknesses of graphene layers. For the investigated region, 30% of the total area contains layers with a thickness of 2 monolayers, while the rest is represented by monolayer graphene. Thus, the electrochemical adsorption of lead adatoms is expected both on monolayer graphene and on bilayer graphene. Fig. 1 displays typical Raman scattering spectra before and after the metal deposition. The analysis of Raman spectra of the sample before electrochemical treatment shows that the Raman map is taken entirely from the monolayer graphene region, whereas the map after Pb electrodeposition covers both monolayer and bilayer regions.

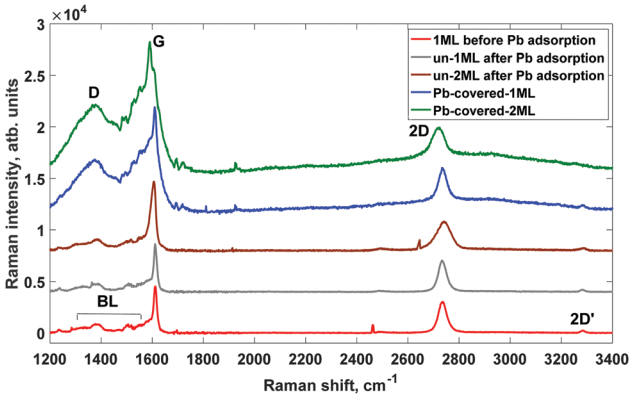

Fig. 1 Typical Raman spectra of epitaxial graphene on 6H-SiC(0001) before and after Pb electrodeposition. It should be noted that the Raman spectra were taken in different sample areas before and after electrochemical treatment. BL denotes the contribution of the buffer layer in the spectrum, which overlaps with the G peak near 1610 cm^{-1}.

A representative spectrum corresponding to a monolayer epitaxial graphene (red curve, Fig. 1) before Pb electrodeposition shows characteristic spectral features at 1611, 2735 and 3283 cm^{-1} (corresponding to G,[23] 2D[24] and 2D′ [25] modes, respectively) as well as a band containing two broad contributions peaking at about 1375 and 1600 cm^{-1}. This latter band represents the contribution of the buffer layer (BL) to the Raman spectrum of epitaxial graphene.[10] We do not detect any Raman signal from the defect-related D mode,[26] pointing to the high crystalline quality of the graphene layers before electrochemical treatment. The absence of the D line also means that a very small fraction of the intrinsic defects is available as effective reaction sites for lead nucleation. It is believed that only active sites belonging to the basal plane (bridge sites) and edge-plane sites can provide the local electron exchange between Pb and graphene. After Pb adsorption, the Raman spectra are measured on monolayer and bilayer graphene regions. There are two types of spectra in the processed sample. One type is represented by the Raman spectra of the bare graphene (graphene regions, which are not covered by adsorbates, see the grey and marron curves in Fig. 1), while the other type of spectra corresponds to graphene occupied by adsorbed metal adatoms (blue and green curves in Fig. 1). Such adsorbates can interact with graphene and change its vibrational properties. A considerable red-shift of the G mode (−15 cm^{-1} for both 1 ML and 2 ML regions in the displayed spectra, respectively) and an increase of its FWHM (+53 cm^{-1} and +42 cm^{-1} for both 1 ML and 2 ML regions in the displayed spectra, respectively) are observed after Pb deposition, which is related to the changes in graphene surface chemistry due to the nonuniform distribution of the individual Pb species and metal clusters attached to the reactive sites. Using DFT calculations, we found that adsorbed Pb atoms tend to occupy the bridge sites (the centre of the C–C bond) of the sp^2 conjugated graphene lattice, acting as electron-donating dopants. We performed Mulliken population analysis and determined the Mulliken charges for each atom in graphene before and after interaction with Pb species. As can be seen in Fig. 2, the Pb atom

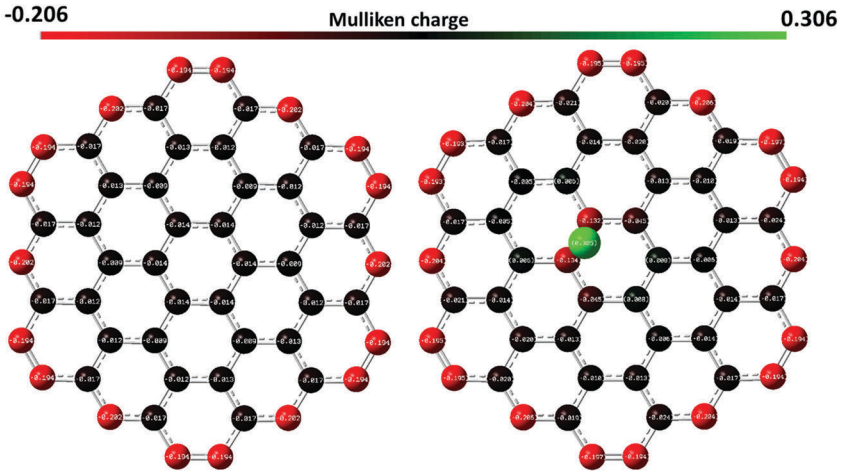

Fig. 2 The Mulliken partial atomic charges on carbon atoms in the pristine graphene (left panel) and on the carbon and Pb atoms in the interacting complex (right corner) calculated at the PBE1PBE-D3/6-311G(d,p)/SDD level.

has a charge of +0.3, while the charges on the carbon species belonging to the bridge site of graphene become more negative compared to the same atoms in pristine graphene, indicating that the graphene accepts electrons from the lead atom (n-type doping).

To gain more insights into the charge transfer mechanism, we also calculated the charge density difference by using the following equation:[27]

$$\Delta\rho = \rho_{\mathrm{Pb@Gr}} - \rho_{\mathrm{Gr}} - \rho_{\mathrm{Pb}} \quad (1)$$

where $\rho_{\mathrm{Pb@Gr}}$, ρ_{Gr}, and ρ_{Pb} are the total charge densities of the interacting structure, the isolated graphene, and the isolated Pb atom, respectively. As shown in Fig. 3, the charge transfer occurs from the Pb adatom to the graphene near the adsorption site. Taking the aforementioned results into account, we can argue that the doping effect is caused by the formation of a hybrid charge transfer complex.

It is important to note that electron doping should result in a blue shift of the G line and a decrease in its half-width.[28] In our case, the red-shift of the G line after Pb adsorption can be understood in terms of the local strain model[29] and the broadening of the G peak width can be related to the local strain variation caused by Pb-induced lattice distortions inside the laser spot.[30] According to the local strain model, which was initially proposed by Zheng *et al.*,[29] the red-shift of the G mode may originate from the charge transfer between the metal species and graphene, as was demonstrated in the case of gold nanoparticles deposited on the graphene surface. Since the total charge transferred from the Pb species to the graphene surface increases upon increasing the amount of Pb atoms, local negatively charged graphene regions occur near the reactive sites. Consequently, two different electrostatic forces are formed. One of them is attractive in nature and tends to bind the Pb atom to the graphene surface (*via* attraction between opposite charges), while another is a repulsive in-plane force between the graphene regions with the same charges, which promotes bending of nano-sized graphene and the appearance of local strain (which is mainly responsible for the red-shift of the G band). We also revealed that the 2D peak position (which is less sensitive to the doping effect compared to the G line) of the 1 ML region is only weakly affected by the adsorbates due to a low doping regime, while the 2D peak of the 2 ML region is red-shifted by 21 cm^{-1} compared with the peak of the uncovered bilayer region.

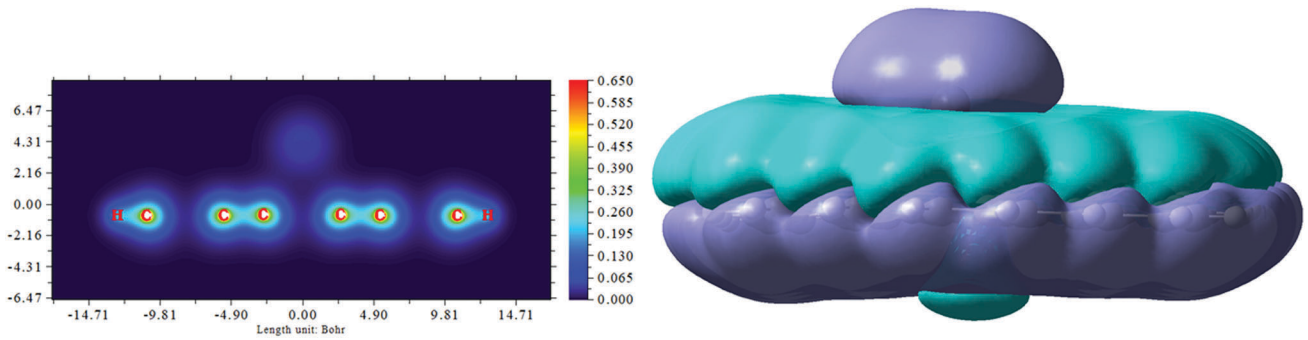

Fig. 3 (left panel) Color-filled maps of electron density of the graphene after interaction with the neutral Pb adatom and (right panel) the electron density difference of the interacting complex. The blue color represents the source of electrons, and the purple color represents where the electrons are going. The contour isovalue is 0.0001.

These findings, altogether, indicate that the Pb species can simultaneously cause n-type doping of graphene and lead to the appearance of inhomogenously distributed local strains.

In the spectra affected by the presence of Pb, in addition to the G and 2D lines, an intense D line is also observed (see the blue and green curves in Fig. 1). Whenever present, the breathing D mode associated with near-*K* point phonons[31] appears at about 1364 cm^{-1}, overlapping with the spectrum of the buffer layer. Its appearance can be explained by adsorbate-induced lattice distortion and the generation of structural defects. Therefore, tracking the changes in this spectral region allows the local Pb adsorption to be probed.

To shed more light on the effect of the Pb deposits on the vibrational properties of epitaxial graphene on SiC, we performed two-dimensional Raman mapping and used statistical analysis to extract information about the spatial uniformity in the graphene properties before and after Pb adsorption (Fig. 4). The comparison of the 2D *vs.* G peak dependencies before and after Pb electrodeposition reveals significant differences, as shown in Fig. 4a. The data points for the pristine graphene sample span primarily along a line with a slope of approximately 2.3 (the fitting procedure is demonstrated in Fig. S1 (ESI†)). This value is in good agreement with the values of ~2.3–2.5, which were frequently observed for purely stressed graphene without the influence of the doping effect, indicating biaxial strain.[32,33] On the other hand, due to the presence of both 1 ML and 2 ML graphene areas inside the mapped region after electrochemical deposition of lead, we observe three different sets of data points corresponding to the 1 ML, 2 ML and Pb-covered graphene regions (see Fig. 4a), respectively. The data points, which are related to the uncovered graphene with different thicknesses, scatter along nearly parallel lines with slopes of approximately 1.9 and 2.2 for the monolayer and bilayer, respectively (linear fitting is presented in Fig. S2, ESI†). Another set of data points (see green asterisks in Fig. 4a) corresponds to the Raman measurement on the graphene sample occupied by adsorbates (all corresponding Raman spectra exhibit a strong defect-related D peak). From the analysis of the statistical spread of these data points, we can infer that the Pb-involved surface reactions over the graphene cause the inhomogeneous distribution of the Raman-spectrum parameters related to the presence of a highly inhomogeneous strain distribution as compared to the pristine graphene. To get more evidence in favour of this assumption, we plotted the dependence of the position of the 2D peak (which is highly sensitive to the strain variations in the graphene layer[34,35]) on its FWHM

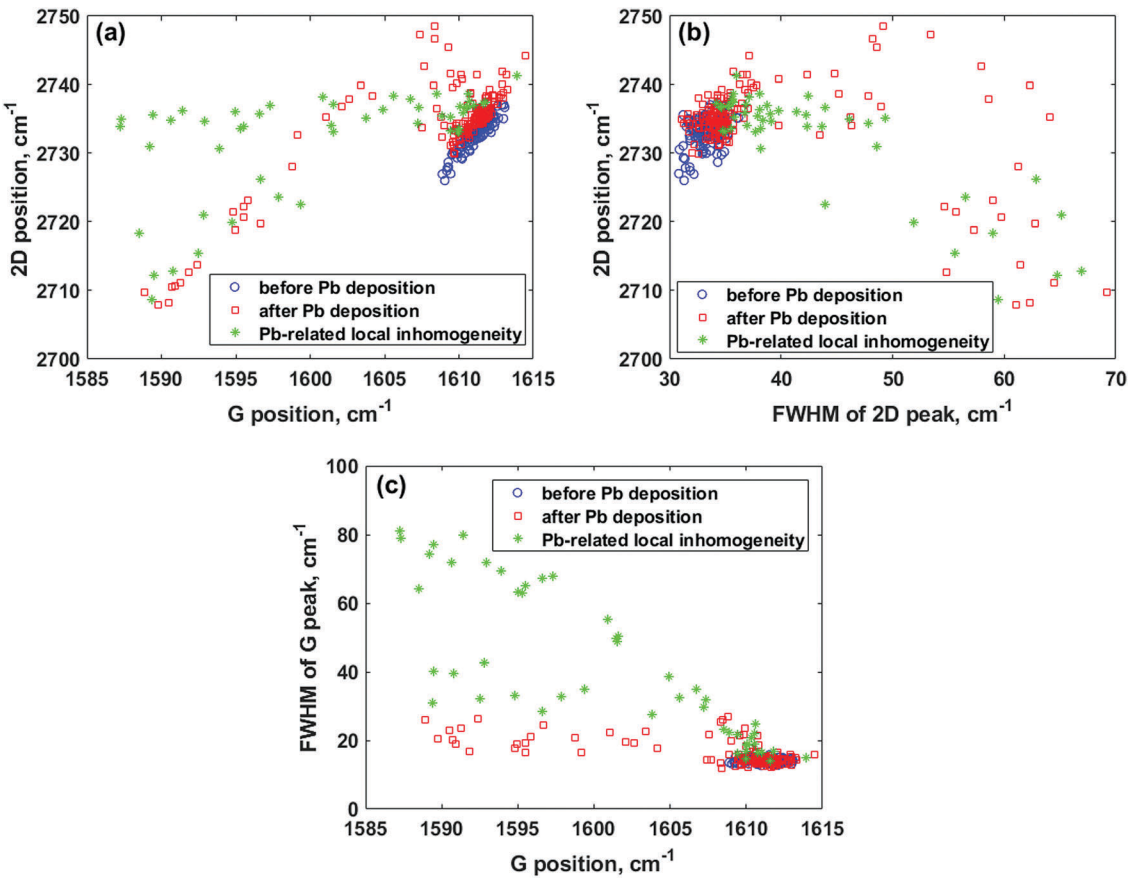

Fig. 4 (a) Correlations between 2D and G peak positions for graphene before Pb electrodeposition (blue circles) and after Pb electrodeposition (red squares) obtained from two-dimensional Raman mapping. (b) Mutual dependence of the 2D peak position and FWHM of the 2D peak for the graphene sample before (blue circles) and after (red squares) interaction with lead. (c) FWHM of the G peak *versus* G peak position before and after Pb adsorption. Green asterisks represent the spectra with enhanced intensity of the defect-induced D line.

value (Fig. 4b). One can see that the pristine graphene before Pb adsorption is narrow and homogeneous within the investigated measurement range, while after Pb adsorption, the 2D peak is significantly broadened. The main source of the 2D peak broadening is most likely due to nanometre-scale local strain fluctuations induced by the occupation of the reactive sites of graphene with electron-donating Pb adsorbates. In Fig. 4c, the FWHM of the G peak is plotted against the position of the G peak. It is clearly seen that the G lines recorded before Pb electrodeposition are narrower compared to those after Pb adsorption, indicating that many random spatial charge fluctuations occur within the laser spot.

A question arises: what is the correlation between the binding ability of the Pb species to graphene and Raman scattering processes in graphene after Pb electrodeposition? To gain an insight into how the question can be addressed, we performed DFT calculations in an attempt to specify the geometrical configuration of the Pb species adsorbed onto graphene and to define the effect of the Pb adatoms on the vibrational properties of the nano-sized graphene. To consider possible realistic adsorption situations, we analyse two contrasting configurations: (i) Pb adatoms are very near to each other and (ii) Pb adatoms are far from each other. Concerning case (i), we found that the Pb adatoms (2, 3 and 4, respectively) were placed close to each other to form dimer, trimer and tetramer structures, with equilibrium distances between the nearest Pb atoms of 2.91 Å, 2.81 Å and 2.97 Å, respectively. An increase in the number of Pb atoms adsorbed on the graphene surface results in a decrease in the total charge transferred between the Pb species and graphene: from $0.3e^-$ (for the one Pb adatom) to $-0.04e^-$ (for the Pb tetramer; in this tetramer, two Pb species have a positive charge, while the others have a negative charge). This is driven by the competition between Pb-sp^2 carbon and Pb–Pb interactions and can be explained by the energetic preference of Pb atoms to clusterize when adsorbed on graphene.[15,36] The changes in the interaction strength manifest themselves in the Raman scattering processes (Fig. 5). In the calculated Raman spectrum of the pristine nano-sized graphene before any interaction with Pb, the most interesting features are observed at 1379 cm^{-1} and 1658 cm^{-1} and can be ascribed to the D and G bands, respectively. The positions of both D and G modes are blue-shifted in comparison to the average experimental values. This discrepancy may originate from the size effect.[37] The spectral features observed in the frequency range between 1300 cm^{-1} and 1360 cm^{-1} and from 1400 to 1630 cm^{-1} are attributed to a mixture of the C–C bond stretching and C–C–H bending vibration modes and in most cases, they are absent in the experimental Raman spectra. The visualization of the D mode demonstrates

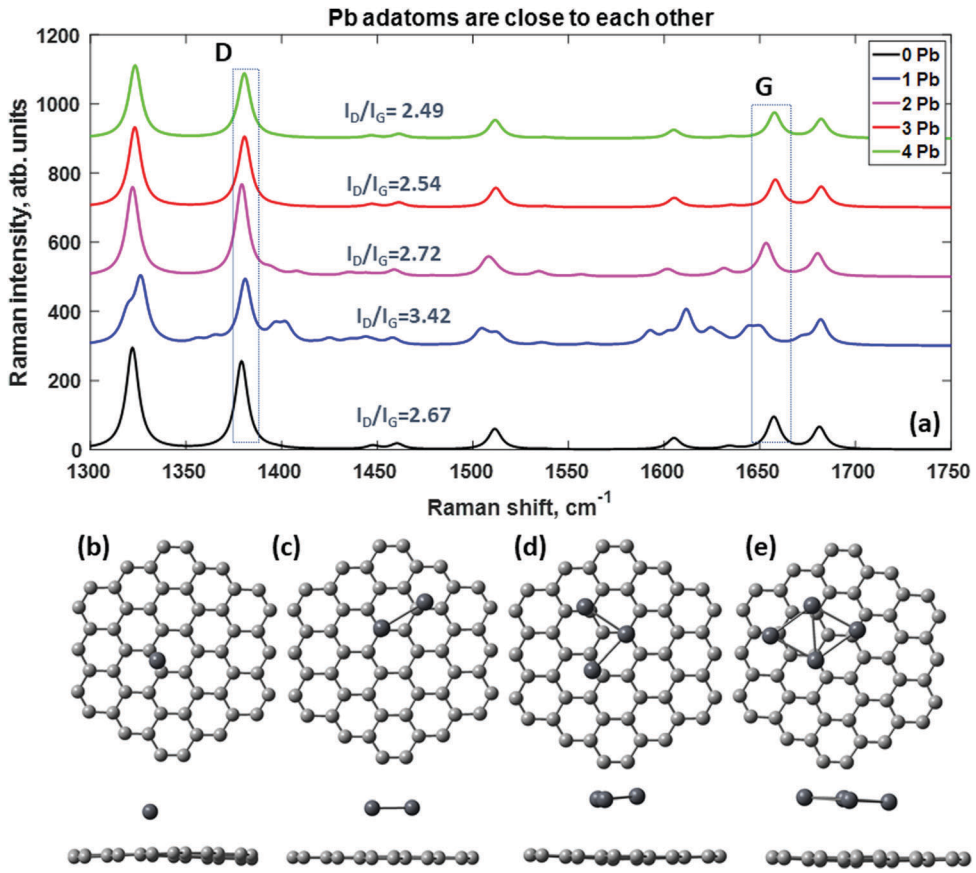

Fig. 5 (a) Calculated Raman spectra of nano-sized graphene before and after interaction with lead (Pb) species. The bottom panel displays optimized geometrical configurations (top view and side view) of the graphene patches after interaction with different numbers of Pb adatoms: (b) 1 Pb, (c) 2 Pb, (d) 3Pb and (e) 4 Pb. It should be mentioned that prior to optimization, the Pb adatoms on the graphene plane were located close to each other.

that it is related to the symmetric ''breathing'' vibration of the hexagonal ring. The strong intensity of this peak is due to the lack of translational symmetry in the model molecule (hence, relaxation of the momentum conservation law) and, consequently, changes in the selection rules, caused by the small size of the zigzag-edged sp^2 graphene fragment. Due to the symmetry of the nano-sized graphene, the G band is doubly degenerate, originating from the iTO phonon mode (1657.34 cm^{-1}) and iLO phonon mode (1658.24 cm^{-1}). This degeneracy is broken after the adsorption of one Pb atom (Fig. 5b) and only the iTO mode contributes to a red-shifted G mode, which occurs at 1650.96 cm^{-1}. We also noticed an increase of the I_D/I_G amplitude ratio after the adsorption event from 2.67 to 3.42, which is in line with the increase of the disorder degree induced by Pb adsorbates. It is generally accepted that the ratio of the intensities of the D and G peaks (I_D/I_G) is correlated with the degree of graphene disorder.[38] This ratio can be used for monitoring the Pb adsorption events, which induce explicit symmetry breaking and activate a strong defect-involving Raman process. Therefore, different I_D/I_G ratios of the nano-sized graphene before and after Pb deposition illustrate the different levels of the defect density. The strong tendency of the Pb atoms to cluster under conditions of critically short metal–metal distances (Fig. 5c–e) implies a decrease of the binding energy, an increase in the Pb atom height above graphene, and a reduction of the charge transfer from Pb adsorbates to the graphene plane. Altogether, this leads to a decrease of n-type doping of graphene and diminishes the strain (C–C bond lengths become closer to an ideal sp^2 C–C bond length of 1.42 Å). Therefore, the Raman spectra of graphene after adsorption of 2, 3 and 4 Pb atoms (which are close to each other) are very similar to the Raman spectrum of the pristine graphene, without any visible shift of the characteristic G and D modes. This finding is important for understanding the experimental results because it suggests that after clustering of Pb atoms, no significant changes are induced in graphene, and the adsorption of large metal clusters on the defect-free graphene basal plane is less likely than the local adsorption of individual Pb adatoms.

Let us consider now the adsorption configurations when Pb adatoms are far from each other. As can be seen in Fig. S3 (ESI†), when the distances between adsorbed Pb atoms on graphene are too long to form clusters, the metal–graphene interaction prevails over the metal–metal interaction and the adsorbates tend to bend the graphene plane. Because of this, the binding energy becomes larger with increasing numbers of the metal atoms, and the total charge transferred from Pb to graphene reaches a maximum value of $1.95e^-$ in the case when four Pb atoms are placed on graphene. All these results reflected a dramatic change in the vibrational properties of the graphene (Fig. S3a, ESI†). It is obvious that after adsorption of the Pb species, the Raman spectra demonstrate a set of bands (forbidden in the case of the pristine graphene) that are related to a combination of the C–C bond stretching, C–C–H angle bending and local vibration modes. Careful analysis of the atom displacements associated with all observed normal modes allows tracking of the behaviour of both D and G modes. The G Raman mode was found to undergo a red shift, while the D peak is blue-shifted. As mentioned before, such behaviour can be explained by the existence of a local strain between graphene and Pb adsorbates. To be more exact, the repulsive interaction between locally randomly distributed negatively-charged graphene regions with nanoscale spatial extents can cause strong tension in graphene. Similar results were reported for Cs,[39] Au,[40] and Fe[41] adatoms on graphene. This assumption is additionally evidenced by the Mulliken atomic charge analysis.[42] Fig. S4 (ESI†) demonstrates the charge density distribution on nano-sized graphene after complexation with Pb neutral adatoms. As can be seen in this figure, the carbon atoms with the highest charge density distribute at the zigzag edges and near the most favourable Pb adsorption sites (bridge sites). This confirms the possibility of the formation of electron puddles and their important role in the appearance of local strains.

DFT calculations also confirmed that individual Pb adsorbates tend to interact with graphene near the edge plane sites. Such behaviour can be explained by the fact the electron density is mainly concentrated around the edges of the graphene, promoting a high electron transfer rate within these regions compared to the electrochemical reactions within the more inert basal plane of graphene. Our results mirror most of the literature data regarding the electrochemical activity of graphene for sensing and electrocatalytic applications, especially with regard to electron transfer reactions, which has mainly been attributed to an enhanced interaction between adsorbates and carbon species near the edge sites. Indeed, the edge-plane sites play a very important role in the electrochemical phenomena occurring at the graphene working electrode.[43–47] In previous studies on graphene electrochemistry, it has been remarked that the edge-to-basal ratio of graphene significantly affects its electrochemical responses towards different analytes.[47–49] The control of this ratio can be achieved, for example, through the intentional formation of multilayer graphene islands on continuous graphene films. As shown in ref. 45, such graphitic islands can dominate the electrochemical response at the graphene electrode. Our studies showed the presence of bilayer patches (more than 30% of overall coverage) in the majority-monolayer graphene sample. We believe that due to such thickness inhomogeneity, a lot of the chemically active sites, namely dangling bonds at the non-passivated bilayer inclusions, are available for reaction with incoming Pb adsorbates, thereby providing the effective charge transfer underlying the electrochemical response of the epitaxial graphene.

3.2 Electrochemical performance of the Gr/SiC electrode

Cyclic voltammetry on the Gr/SiC electrode revealed a double layer region (between 0 V and −0.6 V; Fig. 6a), which featured the absence of any faradaic processes. A higher cathodic polarization (up to −0.9 V) resulted in the appearance of currents of the hydrogen evolution reaction (HER) on Gr/SiC limiting the operational window for metal deposition in a certain aqueous electrolyte (0.1 M $HClO_4$). The presence of lead ions (Fig. 6b) yielded the appearance of cathodic currents of metallic lead deposition

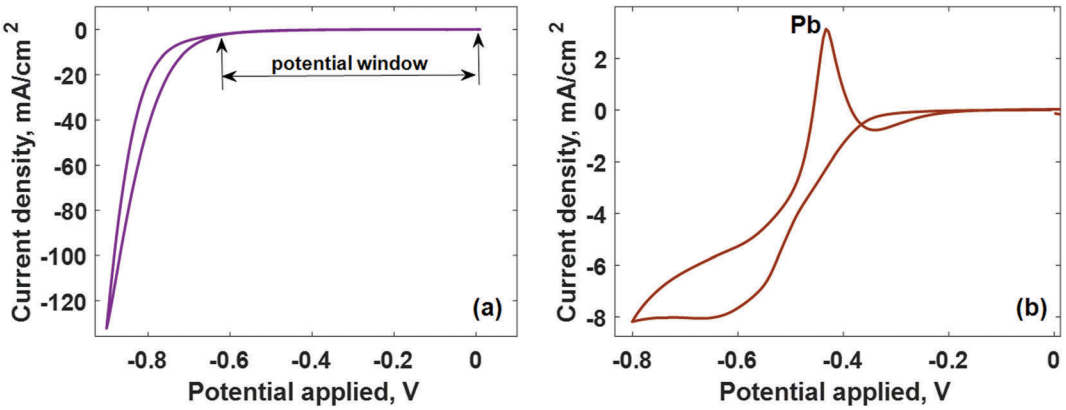

Fig. 6 Lead deposition and ionization on Gr/SiC. Cyclic voltammograms were collected in the absence and in the presence of lead ions ((a) and (b), respectively; 0.1 M $HClO_4$, 0.1 mM $Pb(NO_3)_2$) on Gr/SiC. For (b) the peak is related to reoxidation of Pb^0 to Pb^{2+}, and the back-wave is associated with reduction of Pb^{2+} to Pb^0.

(started at *ca.* −0.35 V), which featured the suppression of background currents due to the higher overpotential of HER on lead. A sharp stripping peak of lead ionisation (−0.43 V) was observed on the anodic scan of cyclic voltammetry, allowing the electrode surface regeneration. The stability of the observed currents during the repetitive potential cycling illustrates the reversibility of the metal deposition and ionisation processes.

3.3 Electrodeposition of lead: chronopotentiometric stripping analysis

To further elucidate the deposition kinetics on the graphene surface, the current transients were recorded as a response of the applied potential pulses of different amplitudes preconditioned at the region of complete lead ionization (−0.2 V). The evolution of the current transient shapes with increasing the cathodic potential pulse amplitude (Fig. S5, ESI,† and Fig. 7) shows a transition from nucleation rate control to reactant diffusion control observed on shorter and longer elapsed times, respectively. The appearance of Pb nuclei accompanied by the current increase due to the nuclei growth is visible at the short-elapsed times. The longer times feature the overlapping of the convergent diffusion profiles of Pb ions resulting in the suppression of the growth rate and a decrease of the recorded currents. The increase of the cathodic polarization with the intensification of the deposition leads to higher current densities (I_{max}) and shorter times until the control transition t_{max} (Fig. 8a).

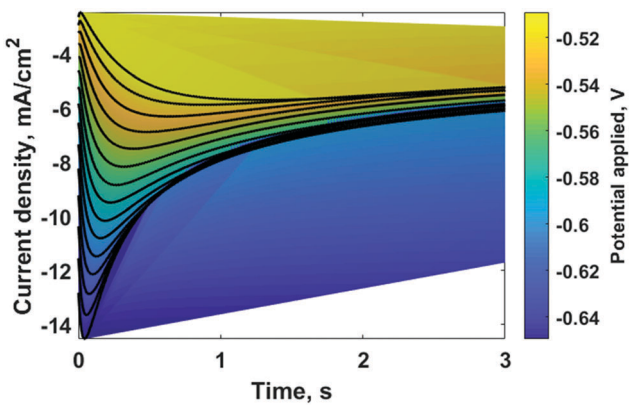

Fig. 7 The evolution of current transients recorded on Gr/SiC at the cathodic potential pulses of different amplitudes (from −0.2 V to −0.64 V; 0.1 mM $Pb(NO_3)_2$ in 0.1 M $HClO_4$).

When the deposition potential is shifted towards more negative potentials, the maximum time, corresponding to the maximum current, tends to become shorter (Fig. 8b), illustrating the potential-driven kinetics of Pb deposition. It is important to note that during the potential stepping, the concentration of the Pb adatoms across the graphene surface reaches its equilibrium value and further accumulation of lead species is completely compensated by their release into the buffer solution. We believe that the accumulation limit is dependent on the concentration of the reactive sites on the graphene surface. This means that the effective control of the nucleation rate can be reached *via* tuning the edge/basal/defect ratios in epitaxial graphene.

In accordance with the Scharifker–Hills theory,[50] there are two possible scenarios of metal deposition depending on the initial surface density of the nucleus. The instantaneous nucleation mechanism is realized if the change of the nucleus density is attainable with the polarization increase. Here, the increase of polarization yields an increase of the nucleation rate up to exhaustion due to the lack of available nucleation sites. At this point, the current corresponding to the instantaneous nucleation obeys the following law:[51]

$$\begin{cases} I(t)_{\text{ins}} = \dfrac{zFD^{1/2}c}{\pi^{1/2}t^{1/2}}[1-\exp(-N_0\pi kDt)] \\ k = \sqrt{\dfrac{(8\pi cM)}{\rho}} \end{cases} \quad (2)$$

where z is the valency of the metal ion (+2 in the case of divalent Pb species), F is the Faraday constant (F = 96 485 C mole^{-1}), c is the Pb concentration ($c = 10^{-7}$ mole cm^{-3}), D is the diffusion coefficient of the lead ions, N_0 is the maximum density of the Pb nucleation centres over the surface of the epitaxial graphene,

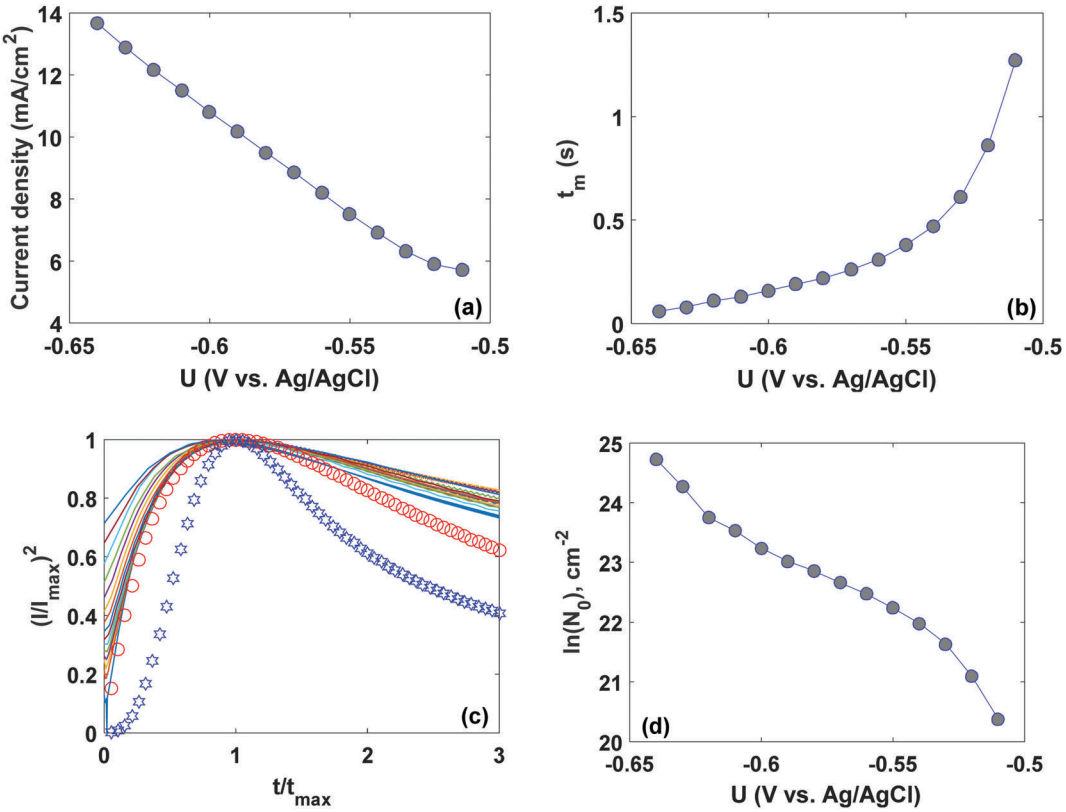

Fig. 8 Dependences of the maximum current density (a) and the time corresponding to the peak current (b) on the applied deposition potential. (c) Comparison of the normalized dimensionless experimental current transient curves with theoretical ones. Blue asterisks correspond to the curve for the progressive nucleation, while the red circles represent the cases of the instantaneous nucleation. (d) ln(N_0) as a function of the applied deposition potential.

M is the molar mass of the Pb, ρ is the density of the deposited species, and t is the time.

In contrast, the progressive nucleation is realized if the initial nucleus density is high enough at the initial stage of growth and the nucleation rate is much higher than the growth rate. This case leads to slow growth due to the overlapped profiles of convergent diffusion of Pb ions. The current transients in the case of progressive nucleation can be described as follows:[50]

$$I(t)_{\mathrm{prog}} = \frac{zFD^{1/2}c}{\pi^{1/2}t^{1/2}}\left[1 - \exp\left(-\frac{2}{3}aN_0\pi kDt^2\right)\right] \qquad (3)$$

where a is the nucleation rate constant. The computed curves derived from eqn (2) and (3) are shown in Fig. 8c, together with the experimental current transients in dimensionless coordinates. It can be seen that the experimental curves for electrodeposition of metallic Pb on Gr/SiC show the best agreement with the dependence computed in the frame of the instantaneous nucleation mechanism, which is consistent with Pb electrodeposition mechanisms reported for copper,[52] silicon surface[51] and tungsten foil.[53]

Further data analysis in the frame of eqn (2) and (3) showed an exponential increase of the number of active nucleation sites (N_0) on Gr/SiC (Fig. 8d), which is typical for an instantaneous nucleation mechanism. According to the SEM results (Fig. S6, ESI†), we observe an inhomogeneous random distribution of micro-sized electrodeposits onto the graphene surface without large nuclei coalescence, which can be ascribed to the low density of the active nucleation sites. It is likely that only the graphene-related intrinsic defects (ripples, wrinkles, vacancies, unsaturated bonds at the edges of the graphene domains, *etc.*) are favourable sites for the electrodeposition of the Pb species while the epitaxial graphene is rather free of the mentioned defects. Bearing in mind the results of DFT calculations (namely, metal clustering due to strong metal–metal interactions weakens the interaction strength between Pb and graphene), we believe that the presence of the large metal-free regions on the graphene surface after Pb electrodeposition can be associated with the release of weakly bonded Pb clusters back into the electrolyte solution.

The data demonstrated in Fig. 7 were utilized for the estimation of the diffusion coefficient of lead ions using the following expression:[51]

$$D = \frac{{I_{\max}}^2 t_{\max}}{0.1629 z^2 F^2 c^2} \qquad (4)$$

It should be mentioned that Pb nuclei grow three-dimensionally at a rate determined by the rate of incorporation of new Pb species. In other words, the nucleation process is fully controlled by the diffusion of Pb ions to the growing centre. Note that the average diffusion coefficient calculated using eqn (4) was about

3.4×10^{-8} cm^2 s^{-1}. In other studies, Pb deposits showed high dispersions in the values of diffusion coefficient depending on the interaction strength with a substrate and illustrating the energetic barriers for surface migration. Indeed, the diffusion coefficient values reported for Pb deposits on glassy carbon, n-Si, tungsten foil, and ITO were found to be 0.89×10^{-5} cm^2 s^{-1},[54] 3.9×10^{-6} cm^2 s^{-1},[51] 3.16×10^{-8} cm^2 s^{-1}[53] and 4.6×10^{-6} cm^2 s^{-1},[55] respectively, illustrating the effect of the interaction strength with a substrate, which depends on the surface conditions. According to the Arrhenius law, a small diffusion coefficient, as observed here, can be attributed to the high activation energy of surface migration.[56,57] As has been shown in our previous work,[15] the surface migration of the neutral Pb species on free-standing graphene requires overcoming high-energy barriers of about 100 meV, which can be explained by the fact that the Pb species tend to reside on bridge sites avoiding the hollow site positions (the centres of the hexagonal rings) on graphene. All experimental details yield atomistic insights into the location of the Pb deposits on graphene.

4. Conclusions

We have presented some insights into the Pb deposition kinetics on epitaxial graphene and the interaction strength between graphene and lead species. An instantaneous nucleation mechanism has been observed for the Pb deposition by electrochemical plating. A small diffusion coefficient (*ca.* 3.4×10^{-8} cm^2 s^{-1}) estimated for the Pb deposits illustrates the high energy barriers for surface migration. This provides appropriate conditions for the electrochemical detection of Pb ions in aqueous solutions, since the incoming Pb individual adatoms can strongly bind to defect-free graphene near the bridge and highly reactive edge-plane sites. The deposition of large metallic clusters happens only at randomly localized extended defect sites providing a high interaction energy, respectively. These defects are most probably created during the electrochemical treatment. Coherently, Raman spectroscopy revealed inhomogenously distributed local strains and randomly distributed negatively-charged in-plane regions induced by Pb deposition. Consistently, computational analysis confirmed the strong interaction (bonding) between individual Pb atoms and graphene and showed that the adsorption of few-atomic Pb clusters on defect-free graphene regions is much less favourable. These observations contribute to the atomistic understanding of metallic Pb phase formation on a graphene monolayer as a technological route towards the selective detection of Pb by electrochemical methods.

Conflicts of interest

There are no conflicts to declare.

Acknowledgements

The authors would like to acknowledge financial support *via* VR grant 621-2014-5805 and SSF (SSF GMT14-0077, SSF RMA15-0024). Dr I. Shtepliuk acknowledges the support from Ångpanneföreningens Forskningsstiftelse (Grant 16-541). All calculations were performed using the supercomputer resources of the Swedish National Infrastructure for Computing (SNIC), National Supercomputing Center (NSC).

References

1 http://www.who.int/ipcs/features/lead.pdf?ua=1.
2 H. Dapul and D. Laraque, Lead poisoning in children, *Adv. Pediatr.*, 2014, **61**(1), 313–333.
3 B. P. Lanphear, R. Hornung, J. Khoury, K. Yolton, P. Baghurst, D. C. Bellinger, R. L. Canfield, K. N. Dietrich, R. Bornschein, T. Greene, S. J. Rothenberg, H. L. Needleman, L. Schnaas, G. Wasserman, J. Graziano and R. Roberts, Low-Level Environmental Lead Exposure and Children's Intellectual Function: An International Pooled Analysis, *Environ. Health Perspect.*, 2005, **113**(7), 894–899.
4 M. Shannon, Severe lead poisoning in pregnancy, *Ambul. Pediatr.*, 2003, **3**(1), 37–39.
5 C. Virojanadara, R. Yakimova, A. A. Zakharov and L. I. Johansson, Large homogeneous mono-/bi-layer graphene on 6H-SiC(0001) and buffer layer elimination, *J. Phys. D: Appl. Phys.*, 2010, **43**, 374010.
6 I. G. Ivanov, J. U. Hassan, T. Iakimov, A. A. Zakharov, R. Yakimova and E. Janzén, *Carbon*, 2014, **77**, 492–500.
7 S. A. Trammell, S. C. Hernández, R. L. M. Ward, D. Zabetakis, D. A. Stenger, D. Kurt Gaskill and S. G. Walton, Plasma-Modified, Epitaxial Fabricated Graphene on SiC for the Electrochemical Detection of TNT, *Sensors*, 2016, **16**(8), 1281.
8 P. Szroeder, N. G. Tsierkezos, M. Walczyk, W. Strupiński, A. Górska-Pukownik, J. Strzelecki, K. Wiwatowski, P. Scharff and U. Ritter, Insights into electrocatalytic activity of epitaxial graphene on SiC from cyclic voltammetry and ac impedance spectroscopy, *J. Solid State Electrochem.*, 2014, **18**, 2555–2562.
9 K. M. Daniels, S. Shetu, J. Staser, J. Weidner, C. Williams, T. S. Sudarshan and M. V. S. Chandrashekhar, Mechanism of Electrochemical Hydrogenation of Epitaxial Graphene, *J. Electrochem. Soc.*, 2015, **162**(4), E37–E42.
10 M. Vagin, A. Sekretaryova, A. Håkansson, T. Iakimov, M. Syväjärvi, R. Yakimova, I. Lundström and M. Eriksson, Monitoring of epitaxial graphene anodization, *Electrochim. Acta*, 2017, **238**, 91–98.
11 I. Shtepliuk, V. Khranovskyy and R. Yakimova, Combining graphene with silicon carbide: synthesis and properties – a review, *Semicond. Sci. Technol.*, 2016, **31**(11), 113004.
12 I. Shtepliuk, T. Iakimov, V. Khranovskyy, J. Eriksson, F. Giannazzo and R. Yakimova, Role of the Potential Barrier in the Electrical Performance of the Graphene/SiC Interface, *Crystals*, 2017, **7**(6), 162.
13 I. Shtepliuk, J. Eriksson, V. Khranovskyy, T. Iakimov, A. L. Spetz and R. Yakimova, Monolayer graphene/SiC Schottky barrier diodes with improved barrier height

uniformity as a sensing platform for the detection of heavy metals, *Beilstein J. Nanotechnol.*, 2016, **7**, 1800–1814.
14 N. Kanani, *Electroplating Basic Principles, Processes and Practice*, Elsevier Kidlington, Oxford, 2004.
15 I. Shtepliuk, N. M. Caffrey, T. Iakimov, V. Khranovskyy, I. A. Abrikosov and R. Yakimova, *Sci. Rep.*, 2017, **7**, 3934.
16 I. Shtepliuk, V. Khranovskyy and R. Yakimova, Insights into the origin of the excited transitions in graphene quantum dots interacting with heavy metals in different media, *Phys. Chem. Chem. Phys.*, 2017, **19**, 30445–30463.
17 R. Yakimova, T. Iakimov and M. Syväjärvi, *Inventors. Process for growth of graphene*, *US Pat.*, US9150417B2, 2015.
18 I. G. Ivanov, J. Hassan, T. Iakimov, A. A. Zakharov, R. Yakimova and E. Janzén, Layer-number determination in graphene on SiC by reflectance mapping, *Carbon*, 2014, **77**, 492–500.
19 M. J. Frisch, G. W. Trucks, H. B. Schlegel, G. E. Scuseria, M. A. Robb and J. R. Cheeseman, *et al.*, *Gaussian 09, Revision D.01*, Gaussian Inc., Wallingford CT, 2009.
20 G. Compagnini, G. Forte, F. Giannazzo, V. Raineri, A. La Magna and I. Deretzis, Ion beam induced defects in graphene: Raman spectroscopy and DFT calculations, *J. Mol. Struct.*, 2011, **993**, 506–509.
21 J. P. Perdew, K. Burke and M. Ernzerhof, Generalized gradient approximation made simple, *Phys. Rev. Lett.*, 1996, **77**, 3865–3868.
22 J. M. L. Martin and A. Sundermann, Correlation consistent valence basis sets for use with the Stuttgart–Dresden–Bonn relativistic effective core potentials: the atoms Ga–Kr and In–Xe, *J. Chem. Phys.*, 2001, **114**, 3408–3420.
23 F. Tuinstra and J. L. Koenig, Raman spectrum of graphite, *J. Chem. Phys.*, 1970, **53**, 112.
24 A. C. Ferrari, J. C. Meyer, V. Scardaci, C. Casiraghi, M. Lazzeri, F. Mauri, S. Piscanec, D. Jiang, K. S. Novoselov, S. Roth and A. K. Geim, Raman Spectrum of Graphene and Graphene Layers, *Phys. Rev. Lett.*, 2006, **97**, 187401.
25 R. Rao, D. Tishler, J. Katoch and M. Ishigami, Multiphonon Raman scattering in graphene, *Phys. Rev. B: Condens. Matter Mater. Phys.*, 2011, **84**, 113406.
26 M. A. Pimenta, G. Dresselhaus, M. S. Dresselhaus, L. G. Cancado, A. Jorio and R. Saito, *Phys. Chem. Chem. Phys.*, 2007, **9**, 1276–1291.
27 C.-S. Guo, L.-B. Luo, G.-D. Yuan, X.-B. Yang, R.-Q. Zhang, W.-J. Zhang and S.-T. Le, Surface Passivation and Transfer Doping of Silicon Nanowires, *Angew. Chem., Int. Ed.*, 2009, **48**, 9896–9900.
28 A. Das, S. Pisana, B. Chakraborty, S. Piscanec, S. K. Saha, U. V. Waghmare, K. S. Novoseliv, H. R. Krishnamurthy, A. K. Geim, A. C. Ferrari and A. K. Sood, Monitoring dopants by Raman scattering in an electrochemically top-gated graphene transistor, *Nat. Nanotechnol.*, 2008, **3**, 210–215.
29 X. Zheng, W. Chen, G. Wang, Y. Yu, S. Qin, J. Fang, F. Wang and X.-A. Zhang, The Raman redshift of graphene impacted by gold nanoparticles, *AIP Adv.*, 2015, **5**, 057133.
30 N. Ali, W. I. Milne, C. S. Ozkan, S. Mitura and J. L. Gervasoni, *Graphene science handbook: electrical and optical properties*, CRC Press, Taylor & Francis Group, 2016.
31 L. G. Cancado, K. Takai, T. Enoki, M. Endo, Y. A. Kim, H. Mizusaki, A. Jorio, L. N. Coelho, R. Magalhaes-Paniago and M. A. Pimenta, General equation for the determination of the crystallite size La of nanographite by Raman spectroscopy, *Appl. Phys. Lett.*, 2006, **88**, 163106.
32 T. M. G. Mohiuddin, A. Lombardo, R. R. Nair, A. Bonetti, G. Savini, R. Jalil, N. Bonini, D. M. Basko, C. Galiotis, N. Marzari, K. S. Novoselov, A. K. Geim and A. C. Ferrari, Uniaxial Strain in Graphene by Raman Spectroscopy: G Peak Splitting, Gruneisen Parameters, and Sample Orientation, *Phys. Rev. B: Condens. Matter Mater. Phys.*, 2009, **79**, 205433.
33 J. E. Lee, G. Ahn, J. Shim, Y. S. Lee and S. Ryu, Optical separation of mechanical strain from charge doping in graphene, *Nat. Commun.*, 2012, **3**, 1024.
34 C. Neumann, S. Reichardt, P. Venezuela, M. Drögeler, L. Banszerus, M. Schmitz, K. Watanabe, T. Taniguchi, F. Mauri, B. Beschoten, S. V. Rotkin and C. Stampfer, Raman spectroscopy as probe of nanometre-scale strain variations in graphene, *Nat. Commun.*, 2015, **6**, 8429.
35 T. Lee, F. A. Mas'ud, M. J. Kim and H. Rho, Spatially resolved Raman spectroscopy of defects, strains, and strain fluctuations in domain structures of monolayer graphene, *Sci. Rep.*, 2017, **7**, 16681.
36 X. Liu, C.-Z. Wang, M. Hupalo, H.-Q. Lin, K.-M. Ho and M. C. Tringides, Metals on Graphene: Interactions, Growth Morphology, and Thermal Stability, *Crystals*, 2013, **3**, 79–111.
37 S. Kim, D. H. Shin, C. O. Kim, S. S. Kang, S. S. Joo, S.-H. Choi1, S. W. Hwang and C. Sone, Size-dependence of Raman scattering from graphene quantum dots: interplay between shape and thickness, *Appl. Phys. Lett.*, 2013, **102**, 053108.
38 L. G. Cançado, A. Jorio, E. H. Martins Ferreira, F. Stavale, C. A. Achete, R. B. Capaz, M. V. O. Moutinho, A. Lombardo, T. S. Kulmala and A. C. Ferrari, Quantifying Defects in Graphene via Raman Spectroscopy at Different Excitation Energies, *Nano Lett.*, 2011, **11**(8), 3190–3196.
39 C. L. Song, B. Sun, Y. L. Wang, Y. P. Jiang, L. L. Wang, K. He, X. Chen, P. Zhang, X. C. Ma and Q. K. Xue, Charge-Transfer-Induced Cesium Superlattices on Graphene, *Phys. Rev. Lett.*, 2012, **108**, 156803.
40 Z. T. Luo, L. A. Somers, Y. Dan, T. Ly, N. J. Kybert, E. J. Mele and A. T. C. Johnson, Size-Selective Nanoparticle Growth on Few-Layer Graphene Films, *Nano Lett.*, 2010, **10**, 777–781.
41 S. M. Binz, M. Hupalo, X. J. Liu, C. Z. Wang, W. C. Lu, P. A. Thiel, K. M. Ho, E. H. Conrad and M. C. Tringides, High Island Densities and Long Range Repulsive Interactions: Fe on Epitaxial Graphene, *Phys. Rev. Lett.*, 2012, **109**, 026103.
42 R. S. Mulliken, Electronic Population Analysis on LCAO-MO Molecular Wave Functions. I, *J. Chem. Phys.*, 1955, **23**, 1833.
43 D. K. Kampouris and C. E. Banks, Exploring the physico-electrochemical properties of graphene, *Chem. Commun.*, 2010, **46**, 8986–8988.

44 M. Pumera, A. Ambrosi, A. Bonanni, E. L. K. Chng and H. L. Poh, Graphene for electrochemical sensing and biosensing, *TrAC, Trends Anal. Chem.*, 2010, **29**, 954–965.

45 D. A. C. Brownson and C. E. Banks, CVD graphene electrochemistry: the role of graphitic islands, *Phys. Chem. Chem. Phys.*, 2011, **13**, 15825–15828.

46 D. A. C. Brownson, M. Gomez-Mingot and C. E. Banks, CVD graphene electrochemistry: biologically relevant molecule, *Phys. Chem. Chem. Phys.*, 2011, **13**, 20284–20288.

47 D. A. C. Brownson, L. J. Munro, D. K. Kampouris and C. E. Banks, Electrochemistry of graphene: not such a beneficial electrode material?, *RSC Adv.*, 2011, **1**, 978–988.

48 M. S. Goh and M. Pumera, Single-, Few-, and Multilayer Graphene Not Exhibiting Significant Advantages over Graphite Microparticles in Electroanalysis, *Anal. Chem.*, 2010, **82**, 8367–8370.

49 W. Yuan, Y. Zhou, Y. Li, C. Li, H. Peng, J. Zhang, Z. Liu, L. Dai and G. Shi, The edge- and basal-plane-specific electrochemistry of a single-layer graphene sheet, *Sci. Rep.*, 2013, **3**, 2248.

50 B. Scharifker and G. Hills, Theoretical and experimental studies of multiple nucleation, *Electrochim. Acta*, 1983, **28**, 879.

51 C. Ziegler, R. I. Wielgosz and D. M. Kolb, Pb deposition on n-Si(111) electrodes, *Electrochim. Acta*, 1999, **45**, 827–833.

52 F. Nasirpouri, On the electrodeposition mechanism of Pb on copper substrate from a perchlorate solution studied by electrochemical quartz crystal microbalance, *Ionics*, 2011, **17**, 331–337.

53 W. He, A. Liu, J. Guan, Z. Shi, B. Gao, X. Hu and Z. Wang, Pb electrodeposition from PbO in the urea/1-ethyl-3-methylimidazolium chloride at room temperature, *RSC Adv.*, 2017, **7**, 6902.

54 T. Store, G. M. Haarberg and R. Tunold, Determination of diffusion coefficients of depositing ions in molten chlorides by transient electrochemical techniques, *J. Appl. Electrochem.*, 2000, **30**, 1351–1360.

55 L. O. S. Bulhoes and L. H. Mascaro, Electrochemical nucleation of lead and copper on indium-tin oxide electrodes, *J. Solid State Electrochem.*, 2004, **8**, 238–243.

56 H. Groult, H. El Ghallali, A. Barhoun, E. Briot, L. Perrigaud, S. Hernandorena and F. Lantelme, Preparation of Co–Sn alloys by electroreduction of Co(II) and Sn(II) in molten LiCl–KCl, *Electrochim. Acta*, 2010, **55**, 1926.

57 L. Li, Z. Shi, B. Gao, J. Xu, X. Hu and Z. Wang, Electrochemical Behavior of Carbonate Ion in the LiF–NaF–Li_2CO_3 System, *Electrochemistry*, 2014, **82**, 1072.